

PI-Net: A Deep Learning Approach to Extract Topological Persistence Images

Anirudh Som*, Hongjun Choi*, Karthikeyan Natesan Ramamurthy[†], Matthew Buman⁺, Pavan Turaga*

*Geometric Media Lab, Arizona State University, Tempe, AZ, USA

[†]IBM Research, Yorktown Heights, NY, USA

⁺College of Health Solutions, Arizona State University, Phoenix, AZ, USA

{anirudh.som, hchoi71}@asu.edu, knatesa@us.ibm.com, {matthew.buman, pavan.turaga}@asu.edu

Abstract

Topological features such as persistence diagrams and their functional approximations like persistence images (PIs) have been showing substantial promise for machine learning and computer vision applications. Key bottlenecks to their large scale adoption are computational expenditure and difficulty in incorporating them in a differentiable architecture. We take an important step in this paper to mitigate these bottlenecks by proposing a novel one-step approach to generate PIs directly from the input data. We propose a simple convolutional neural network architecture called PI-Net that allows us to learn mappings between the input data and PIs. We design two separate architectures, one designed to take in multi-variate time series signals as input and another that accepts multi-channel images as input. We call these networks Signal PI-Net and Image PI-Net respectively. To the best of our knowledge, we are the first to propose the use of deep learning for computing topological features directly from data. We explore the use of the proposed method on two applications: human activity recognition using accelerometer sensor data and image classification. We demonstrate the ease of fusing PIs in supervised deep learning architectures and speed up of several orders of magnitude for extracting PIs from data. Our code is available at <https://github.com/anirudhsom/PI-Net>.

1. Introduction

Deep learning over the past decade has had tremendous impact in computer vision, natural language processing, machine learning, and healthcare. Among other approaches, convolutional neural networks (CNNs) in particular have received great attention and interest from the computer vision community. This is attributed to the fact that they are able to exploit the local temporal and spatial correlations that exist in 1-dimensional (1D) sequential time-series signals, 2-dimensional (2D) data like images, 3-dimensional (3D) data like videos, and 3D objects.

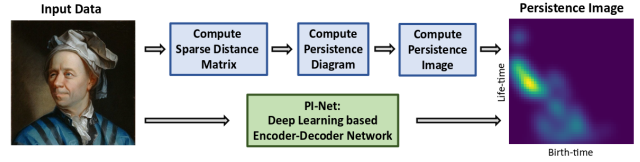


Figure 1. Illustration of the proposed PI-Net model to directly compute topological features called persistence images.

In this paper, we refer to these type of data as *input data*. CNNs also have far less learnable parameters than their fully-connected counterparts, making them less prone to over-fitting and have shown state-of-the-art results in applications like image classification, object detection, scene recognition, fine-grained categorization and action recognition [26, 20, 50, 51, 52]. Apart from being good at learning mappings between the input and corresponding class labels, deep learning frameworks are also efficient in discovering mappings between the input data and other output feature representations [45, 47, 28, 16, 13].

While methods for learning features from scratch and mapping data to desired outputs via neural networks have matured significantly, relatively less attention has been paid to invariance to nuisance low-level transforms like Gaussian noise, blur and affine transformations. Topological data analysis (TDA) methods are popularly used to characterize the *shape* of high-dimensional point cloud data using representations such as persistent diagrams (PDs) that are robust to certain types of variations in the data [14]. The shape of the data is quantified by properties such as connected components, cycles, high-dimensional holes, level-sets and monotonic regions of functions defined on the data [14]. Topological properties are those invariants that do not change under smooth deformations like stretching, bending and rotation, but without tearing or gluing surfaces. These attractive traits of TDA has renewed interest in this area for answering various fundamental questions, including those dealing with interpretation, generalization, model selection, stability, and convergence [19, 6, 34, 32, 18, 17].

A lot of work has gone into utilizing topological representations efficiently in large-scale machine learning [3, 5,

35, 30, 33, 1, 40]. However, bottlenecks such as computational load involved in discovering topological invariants as well as a lack of a differentiable architecture remain. In this paper we propose a deep learning approach to learning approximate mappings between data and their topological feature representations, efficiently and using a differentiable architecture. The gist of our idea is illustrated in figure 1 and the main contributions are listed below.

Contributions: (1) We propose a novel differentiable neural network architecture called *PI-Net*, to extract topological representations. In this paper we focus on persistence images (PIs) as the desired topological feature. (2) We provide two simple CNN-based architectures called *Signal PI-Net* that takes in multi-variate 1D sequential data and *Image PI-Net* that takes in multi-channel 2D image data. (3) We also employ transfer learning strategies to train the proposed *PI-Net* model on a source dataset and use it on a target dataset. (4) Through our experiments on human activity recognition using accelerometer sensor data and image classification on standard image datasets, we show the effectiveness of the generated approximations for PIs and compare their performance to PIs generated using TDA approaches. We also explore the benefits of concatenating PIs with features learnt using deep learning methods like *Alexnet* [26], *Network-in-Network* [27] for image classification and test their robustness to different noise variations. Our code is available at <https://github.com/anirudhsom/PI-Net>.

The rest of the paper is outlined as follows: Section 2 discusses related work. Section 3 provides the necessary background on TDA and PIs. In Section 4 we describe the proposed framework in detail and in Section 5 we describe the experimental results. Section 6 concludes the paper.

2. Related Work

Although the formal beginnings of topology is already a few centuries old dating back to Euler, algebraic topology has seen a revival in the past decade with the advent of computational tools and software [36, 2, 4]. Arguably the most popular topological summary is the persistence diagram (PD), which is a multi-set of points in a 2D plane that quantifies the *birth* and *death* times of topological features such as k -dimensional holes of sub-level sets of a function defined on a point cloud [15]. This simple summary has resulted in adoption of topological methods for various applications [31, 43, 8, 11, 10, 23, 39, 44]. However, TDA methods suffer from two major limitations. First, it is computationally very taxing to extract PDs. The computational load increases with the dimensionality of the data being analyzed. The second obstacle is that a PD is a multi-set of points, making it impossible to use machine learning or deep learning frameworks directly on the space of PDs. Efforts have been made to tackle the second issue by attempting to map PDs to spaces that are more favorable for

machine learning tools [3, 5, 35, 30, 33, 1, 40]. To alleviate the first problem, in this paper we propose a simple one-step differentiable architecture called *PI-Net* to compute the desired topological feature representation, specifically persistence images (PIs). To the best of our knowledge, we are the first to propose the use of deep learning for computing PIs directly from data.

Our motivation to use deep learning stems from its successful use to learn mappings between input data and different feature representations [45, 47, 28, 16, 13]. However, deep learning and TDA did cross paths before but not in the same context as what we propose in this paper. TDA methods have been used to study the topology [19, 6], algorithmic complexity [34], behavior [18] and selection [32] of deep learning models. Efforts have also been made to use topological feature representations either as inputs or fused with features learned using neural network models [12, 24, 7]. Later in Section 5, we too show experimental results on fusing generated PIs with deep learning frameworks for action recognition and image classification tasks.

3. Background

Persistence Diagrams: Consider a graph $\mathcal{G} = \{\mathcal{V}, \mathcal{E}\}$ constructed from data projected onto a high-dimensional point-cloud space. Here, \mathcal{V} is the set of $|\mathcal{V}|$ nodes and \mathcal{E} denotes the neighborhood relations defined between the samples. Topological properties of the graph’s shape can be estimated by first constructing a simplicial complex \mathcal{S} over \mathcal{G} . \mathcal{S} is defined as $\mathcal{S} = (\mathcal{G}, \Sigma)$, with Σ being a family of non-empty level sets of \mathcal{G} , with each element $\sigma \in \Sigma$ is a simplex [15]. This falls under the realm of *persistent homology* when we are interested in summarizing the k -dimensional holes present in the data. The simplices are constructed using the ϵ -neighborhood rule [15]. It is also possible to quantify the topology induced by a function g defined on the vertices of a graph \mathcal{G} by studying the topology of its sub-level or super-level sets. Since $g : \mathcal{V} \rightarrow \mathbb{R}$, this is referred to as *scalar field topology*. In either case, PDs provide a simple way to summarize the birth vs death time information of the topological feature of interest. Birth-time (b) refers to the scale at which the feature was formed and death-time (d) refers to the scale at which it ceases to exist. The difference between d and b gives us the life-time or persistence and is denoted by $l = |d - b|$. Each PD is a multi-set of points (b, d) in \mathbb{R}^2 . Interested readers can refer to the following papers to learn more about the properties of the space of PDs [14, 15].

Persistence Images: A PI is a finite-dimensional vector representation of a PD [1] and can be computed through the following series of steps. First we map the PD to an integrable function $\rho : \mathbb{R} \rightarrow \mathbb{R}^2$ called a persistence surface. The persistence surface ρ is defined as a weighted sum of Gaussian functions that are centered at each point in

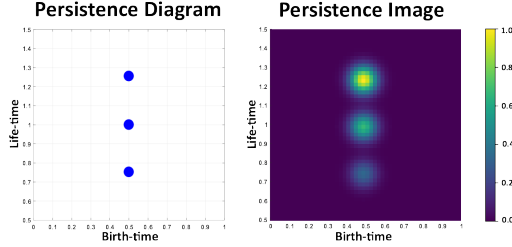


Figure 2. Illustration of a PD and its weighted PI for three points with same birth-times but different life-times. Due to the weighting function points with higher life-time appear more brighter.

the PD. Next, a discretization of a subdomain of the persistence surface is done which results in a grid. Finally, the PI is obtained by integrating the persistence surface over each grid box, giving us a matrix of pixel values. An interesting aspect when computing PIs is the broad range of weighting functions to choose from, to weight the Gaussian functions. Typically, points of high persistence or lifetime are perceived to be more important than points of low persistence. In such cases one may select the weighting function to be non-decreasing with respect to the persistence value of each point in the PD. Adams *et al.* also talk about the stability of persistence images with respect to the 1-Wasserstein distance between PDs [1]. Figure 2 shows an example of a PD and its PI that is weighted by its life-time.

Convolutional Neural Networks: CNNs were inspired from the hierarchical organization of the human visual cortex [21] and consist of many intricately interconnected layers of neuron structures serving as the basic units to learn, extract both low-level and high-level features from images. CNNs are particularly more attractive and powerful compared to their connected counterparts because CNNs are able to exploit the spatial correlations present in natural images and each convolutional layer has far less trainable parameters than a fully-connected layer. Several sophisticated CNN architectures have been proposed in the last decade, for example *AlexNet* [26], *Network-in-Network* [27], *VGG* [38], *GoogleNet* [42], *ResNet* [22], etc. Some of these designs are known to surpass humans for object recognition tasks [37]. Apart from discovering features from scratch for classification tasks, CNNs are also popular for learning mappings between input and other feature representations [45, 47, 28, 16, 13]. This motivates us to design simple CNN models for the task of learning mappings between the data and their PI representations. We would like to direct interested readers to the following survey paper to know more about different CNN architectures [41].

Learning Strategies: Here we will briefly talk about the two learning strategies namely: supervised learning and transfer learning. We employ these strategies to train the proposed *PI-Net* model. *Supervised Learning* is concerned with learning complex mappings from X to Y when many pairs of (x, y) are given as training data, with $x \in X$ being

the input data and $y \in Y$ being the corresponding label or feature representation. In a classification setting Y corresponds to a fixed set of labels. In a regression setting, the output Y is either a real number or a set of real numbers. In this paper our problem falls under the regression category as we try to learn a mapping between the input data and its PI. *Transfer Learning* is a design methodology that involves using the learned weights of a pre-trained model that is trained on a source dataset \mathcal{D}_s for the source task \mathcal{T}_s , to initialize the weights of another model that is fine-tuned using a target dataset \mathcal{D}_t for the target task \mathcal{T}_t [48]. When training a model, abstract feature representations are usually learnt in the initial and middle layers, whereas task-specific features are learnt in the final layers. With transfer learning we only re-train or fine-tune the last layers. This allows us to leverage the source dataset that the model was initially trained on. This is useful in cases where the target dataset is a lot less compared to the source dataset. However, transfer learning only works if the features learned for the source task are generalizable for the target task. In Section 4 we show how transfer learning is employed in our proposed framework.

4. PI-Net Framework

In this section we will first go through the steps to generate the ground-truth PIs and later discuss the proposed network architecture. The two *PI-Net* variants are illustrated in Figure 3. To generate PIs from multi-variate time-series signals we use *Signal PI-Net* and for multi-channel images we use *Image PI-Net*.

4.1. Generating Ground Truth Persistence Images

Data Pre-processing: For uni-variate or multi-variate time-series signals, we consider only fixed-frame signals, *i.e.* signals with fixed number of time-steps, and zero-center them. We standardize the train and test sets such that they have unit variance along each time-step. For images we enforce the pixel value range to be $[0, 1]$.

Computing Persistence Diagrams and Images: We use the *Scikit-TDA* python library [36] and use the *Rips* package for computing PDs. We only focus on extracting PDs of scalar functions on data. When working with 1D sequential data, these offer a way to describe extremal points. For example local minimums give birth to a topological feature (more accurately a 0-order homology group) which then die at local maxima. From our initial investigations we were able to generate PIs which had features of high persistence. We can also extract PDs from an image considering the pixel values to be the function on a 2D plane. However, using this approach we were not able to observe PDs with high persistence features for the image. Instead, we vectorize each image along its rows to form a 1D signal. We then extract PDs for the 1D signal, just as we do for time-series data. For multi-channel color images, we vectorize each

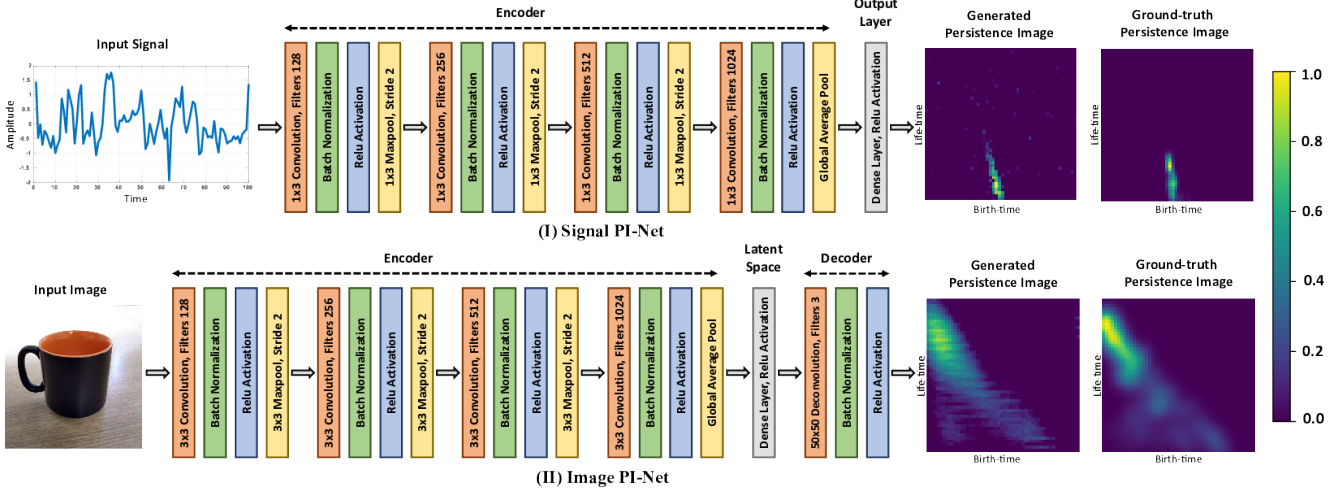


Figure 3. Illustration of the proposed Signal PI-Net (top) and Image PI-Net (bottom) networks to generate PIs directly from the input data.

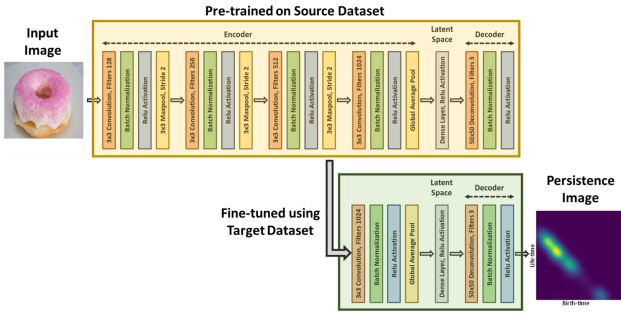


Figure 4. Illustration of transfer learning being used to train the Image PI-Net model. The model is first trained on the source dataset and the last layers are later fine-tuned using the target dataset.

color channel separately and then compute PDs. For example, we reshape a $32 \times 32 \times 3$ color image to get 1024×3 . This small change allowed us to observe more richer PDs that have features with high persistence.

For computing PIs we used the *Persim* package in the *Scikit-TDA* toolbox. In all our experiments we set the grid size of the generated PIs to 50×50 and fit a Gaussian kernel function on each point in the PD. We weight each Gaussian kernel by the life-time of the point. For all time-series datasets we set the standard deviation of the Gaussian kernel to 0.25 and set the birth-time range to $[-10, 10]$. For image datasets we fix the standard-deviation to 0.05 and the birth-time range to $[0, 1]$. Once we compute PIs we normalize each PI by dividing by its maximum intensity value. This forces the intensity values in the PI to lie between $[0, 1]$.

4.2. Network Architecture

Here, we describe the *Signal PI-Net* and *Image PI-Net* architectures. These models are shown in Figure 3 and are designed using Keras with tensorflow backend [9].

Signal PI-Net: The input to the network is a $t \times n$ dimensional time-series signal, where t refers to the number of time-steps or frame size. For a uni-variate signal $n = 1$ and

for a multi-variate signal $n > 1$. For our experiments in Section 5, $t = 100$ and $n = 3$. After the input layer, the encoder block consists of four 1D convolution layers. Except the final convolution layer, all other convolution layers are followed by batch normalization, ReLU activation and Max-pooling. The final convolution layer is followed by batch normalization, ReLU activation and Global-average-pooling. The number of convolution filters is set to 128, 256, 512 and 1024 respectively. However, the convolution kernel size is same for all layers and is set to 3 with stride set to 1. We use appropriate zero padding to keep the output shape of the convolution layer unchanged. For all Max-pool layers, we set the kernel size to 3 and stride to 2. After the encoder block, we pass the global-average-pooled output into a final output dense layer of size $2500 \times n$. The output of the dense layer is subjected to ReLU activation and reshaped to size $50 \times 50 \times n$. As mentioned earlier, we set the height and width of all generated PIs to 50.

Image PI-Net: The input to this network is a $h \times w \times c$ dimensional image, where h, w, c are the image’s height, width and number of channels. The structure of the encoder block is the same as that of the *Signal PI-Net* model. The only difference is that we now use the 2D version of the same layers described earlier. We pass the output of the encoder block into a latent variable layer which consists of a dense layer of size 2500. The output of the latent variable layer is reshaped to 50×50 and is passed into the decoder block. The decoder block consists of one 2D deconvolution layer with kernel size set to 50, stride set to 1, number of filters to c . The output of the deconvolution layer is also zero-padded such that the height and width of the output remains unchanged. The deconvolution layer is followed by a final batch normalization and ReLU activation. The shape of the output we get is $50 \times 50 \times c$.

To employ transfer learning, we first train the Image PI-

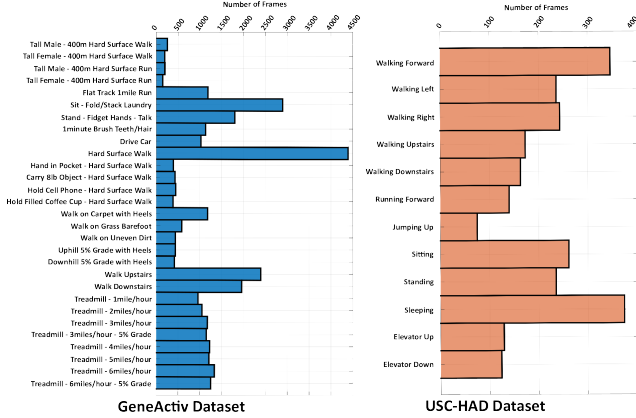


Figure 5. Distribution of the different human-activity classes for the GeneActiv (left) and USC-HAD (right) datasets.

Net model on a source dataset. Next, we fine-tune just the last layers of the model using the target dataset. Specifically, we re-train from the fourth convolution layer with 1024 filters in the Encoder block till the final output layer as shown in Figure 4.

Loss function: The Mean-Squared-Error loss function is used to quantify the deviation of the generated PIs from the ground-truth PIs. The different train and test loss trends for both Signal and Image PI-Net variants is shown in Figure 6.

5. Experiments

This section can be broadly divided into four parts. First we show human activity recognition on two accelerometer sensor datasets: *GeneActiv* [46] and *USC-HAD* [49]. Second, we show improvements for image classification task after fusing PIs obtained traditionally and using the proposed Image PI-Net framework with popular neural network architectures like *Alexnet* [26] and *Network-in-Network* [27]. For image classification we use the following datasets: *CIFAR10* [25] and *SVHN* [29]. Third, we show how the generated PIs can be used to help improve robustness of deep learning models to different noises like blur, translation and Gaussian noise. Finally, we show improvements in computation time for the task of extracting PIs using the proposed method.

5.1. Action Recognition using Accelerometer Data

We conduct this experiment on the following accelerometer datasets: *GeneActiv* [46] and *USC-HAD* [49]. The *GeneActiv* dataset consists of 29 different human-activity classes from 152 subjects. The data was collected at a sampling rate of 100Hz using a GeneActiv sensor, a light-weight, waterproof, wrist-worn tri-axial accelerometer. Please refer to the following paper to know more about the data collection protocol [46]. We extract non-overlapping frames of 10 seconds each, giving us about 31,275 frames. Each frame has a 1000 time-steps. We

Method	GeneActiv	USC-HAD
MLP - PI	46.27±0.28	44.71±1.26
MLP - Signal PI-Net	49.76±0.90	48.21±1.42
MLP - SF [46]	35.48±0.50	31.86±2.47
MLP - SF + PI	47.63±0.43	45.79±0.33
MLP - SF + Signal PI-Net	49.68±0.22	48.68±0.63
1D CNN	56.34±0.89	53.33±1.35
1D CNN + PI	58.68±0.49	55.67±1.03
1D CNN + Signal PI-Net	59.42±0.35	58.56±0.81

Table 1. **Weighted F1 score** classification results for the GeneActiv and USC-HAD datasets. The results shown are the mean \pm standard-deviation values calculated over 5 runs.

roughly use 75% of the frames for the training-set and the rest as test-set. To avoid inducing any bias, we make sure to place all frames from the same subject into either one of the sets. The *USC-HAD* dataset consists of 12 different human-activity classes from 14 subjects. It was collected using the tri-axial MotionNode accelerometer sensor at a sampling rate of 100Hz, with the sensor being placed at the front right hip [49]. Here also we extract 10 second non-overlapping frames resulting in about 2,499 frames. We use frames from the first 8 subjects for the training set and the remaining frames as the test set. Figure 5 show the list of all activity classes and their distribution for both datasets.

Training Signal PI-Net: We train one *Signal PI-Net* model described in Section 4.2 using just the training set of the *GeneActiv* dataset. We set the batch-size to 128 and train the model for a 1000 epochs. The learning rate for the first 300 epochs, second 300 epochs and final 400 epochs was set to 10^{-3} , 10^{-4} and 10^{-5} respectively. The Adam optimizer was used for training the model. We use the Mean-Squared-Error loss function to quantify the overall deviation of the generated PIs from the ground-truth PIs. The training and test loss trends are shown in Figure 6.

For characterizing the time-series signals, we consider three different feature representations: (1) A 19-dimensional feature vector consisting of different statistics calculated over each 10-second frame [46]; (2) Features learnt from scratch using 1D CNNs; (3) Persistence Images generated using the traditional filtration technique and the proposed *Signal PI-Net* model. The 19-dimensional feature vector includes *mean*, *variance*, *root-mean-square* value of the raw accelerations on each of X , Y and Z axes, *pearson correlation coefficients* between X - Y , Y - Z and X - Z time series, *difference between maximum and minimum accelerations* on each axis denoted by dx , dy , dz , and $\sqrt{dx^2 + dy^2}$, $\sqrt{dy^2 + dz^2}$, $\sqrt{dx^2 + dz^2}$, $\sqrt{dx^2 + dy^2 + dz^2}$. From here on out we will refer to this 19-dimensional statistics feature as SF. We use the trained *Signal PI-Net* model to extract PIs for the test set of the *GeneActiv* dataset. We also use the same model to compute PIs for both the training and test sets of the *USC-HAD* dataset. We wanted to see if we could exploit the knowledge learnt by the proposed *Signal PI-Net* model on a source dataset

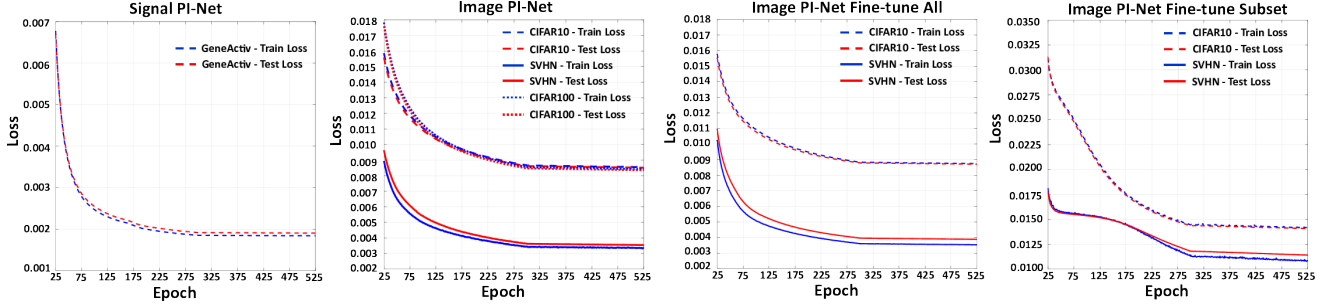


Figure 6. Train - Test loss trends for different PI-Net models. Here, we only show the trends from epochs 25 to 525. The train loss for the Signal PI-Net model starts at about 0.045 and for most Image PI-Net models at around 0.25. Between the epochs 1 and 1000 we see a reduction in the overall loss by about one order of magnitude in all cases.

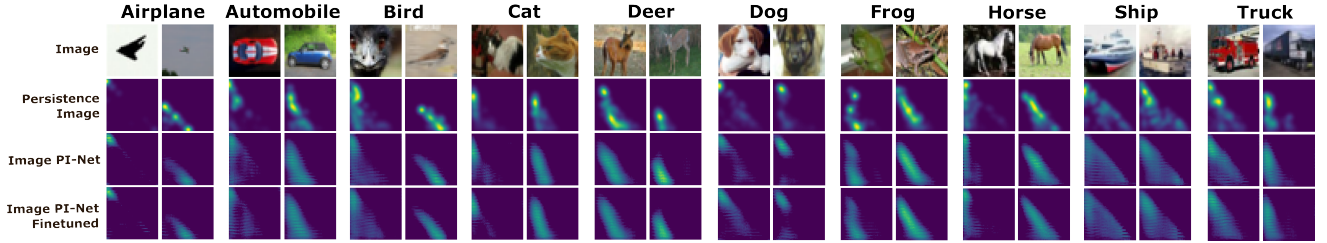


Figure 7. Illustration of sample test images in CIFAR10 (1st row) and their corresponding ground-truth PIs (2nd row), PIs generated using the *Image PI-Net* model (3rd and 4th rows).

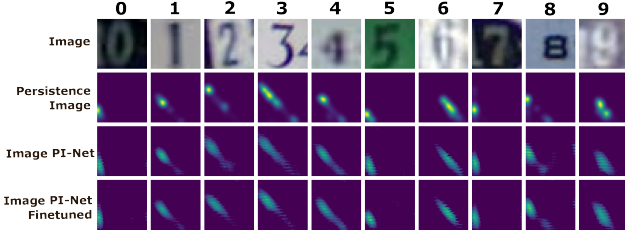


Figure 8. Illustration of sample test images in SVHN (1st row) and their corresponding ground-truth PIs (2nd row), PIs generated using the *Image PI-Net* model (3rd, 4th rows).

(*GeneActiv*) and use it on a target dataset (*USC-HAD*). As seen from Figure 5, there is a huge shift in both the data distribution and end-target classes. This pushes it to the realm of a cross-domain and cross-task learning problem. Cross-domain since for each dataset the accelerometer sensor was placed on different parts of the human body; and cross-task since the class-distribution and end classification task is very different for both datasets.

The weighted F1 score classification results is shown in Table 1. We use a multi-layer-perceptron (MLP) classifier for the SF, PI features and a 1D CNN classifier for the time-series signals. The MLP classifier contains 8 dense layers with ReLU activation and having 1024, 1024, 512, 512, 256, 256, 128, 128 units respectively. To avoid over-fitting, each dense layer is followed by a dropout layer with a dropout rate of 0.2 and a batch-normalization layer. The output layer is another dense layer with Softmax activation and with number of units equal to the number of classes. The 1D CNN classifier consists of 10 CNN layers with number of filters set to 64, kernel size to 3, stride to 1

and the output is zero-padded. Each CNN layer is followed by batch-normalization, ReLU activation and max-pooling layers. For max-pool layers we set the filter size to 3, the stride was set to 1 for every odd layer and 2 for every even layer. For the final CNN layer we use a global-average-pooling layer instead of a max-pool layer. Here too, the output layer consists of a dense layer with softmax activation and number of units equal to number of target classes.

Table 1 shows results for both individual features and different fusion cases. In the table, PI refers to PIs obtained using conventional TDA methods and Signal PI-Net means PIs computed using the proposed *Signal PI-Net* model. We fuse SF and PI features at the input layer before passing into the MLP classifier. For 1D CNNs we fuse the PI features after the global-average-pooling layer. We see improvements in classification results using the proposed *Signal PI-Net* model for both datasets. We would like to remind our readers that the results for *USC-HAD* was obtained using the *Signal PI-Net* model trained on just the *GeneActiv* dataset. This opens doors to further explore the proposed framework on cross-domain, cross-task learning problems. For the 1D CNN case, apart from improving the overall classification accuracy we also notice the standard deviation being reduced after combining PIs. We further provide the confusion matrices for a few of the methods listed in table 1 in the Appendix at the end of the paper.

5.2. Image Classification

We use the following three image datasets for purposes of training different *Image PI-Net* models: *CIFAR10*, *CIFAR100* [25] and *SVHN* [29]. However, we show image

Alexnet [26]		Network-in-Network [27]	
Name	Description	Name	Description
input	32 × 32 RGB image	input	32 × 32 RGB image
conv1a	32 filters, 3×3, pad='same', ReLU	conv1a	192 filters, 5×5, pad='same', ReLU
conv1b	32 filters, 3×3, ReLU	conv1b	160 filters, 1×1, pad='same', ReLU
pool1	Maxpool 2×2	conv1c	96 filters, 1×1, pad='same', ReLU
drop1	Dropout 0.2	pool1	Maxpool 3×3, stride=(2,2), pad='same'
conv2a	64 filters, 3×3, pad='same', ReLU	conv2a	192 filters, 5×5, pad='same', ReLU
conv2b	64 filters, 3×3, ReLU	conv2b	192 filters, 1×1, pad='same', ReLU
pool2	Maxpool 2×2	conv2c	192 filters, 1×1, pad='same', ReLU
drop2	Dropout 0.2	pool2	Maxpool 3×3, stride=(2,2), pad='same'
flatten1	Flatten	conv3a	192 filters, 3×3, pad='same', ReLU
dense1	Fully connected 1024 units, ReLU	conv3b	192 filters, 1×1, pad='same', ReLU
drop3	Dropout 0.2	conv3c	10 filters, 1×1, pad='same', ReLU
dense2	Fully connected 10 units	gavg-pool1	Global Average Pool
output	Softmax	output	Softmax

Table 2. The architecture descriptions for Alexnet (left) and Network-in-Network (right) models.

classification results for only *CIFAR10* and *SVHN*. Both *CIFAR10* and *CIFAR100* contain 60,000 color images, which are split into 50,000 training images and 10,000 test images. The *SVHN* dataset contains 73,257 training images and 26,032 test images. Images have the same shape in all three datasets. The height, width and number of channels for each image is equal to 32, 32 and 3 respectively. Sample test images in each class for the *CIFAR10* and *SVHN* dataset are shown in Figures 7 and 8 respectively.

Training Image PI-Net: We develop two kinds of *Image PI-Net* models based on the datasets we chose as source and target datasets to train the model: (1) In the first kind we set the source and target datasets to be same, *i.e.* we train the Image PI-Net model using the *CIFAR10* or *SVHN* dataset. (2) For the second type, we use the *CIFAR100* dataset as our source dataset and the target datasets are either *CIFAR10* or *SVHN*. Simply put, we employ transfer learning by first training the Image PI-Net model using *CIFAR100* and later use the target dataset to fine-tune the last layers as illustrated in Figure 4. For the second case, we further explore two variations: (2a) Fine-tune the last layers using all samples from the training set of the target dataset; (2b) fine-tune using just a subset *i.e.* 500 images per class in the training set of the target dataset. We will refer to these variants as *Image PI-Net* FA (Fine-tune All) and *Image PI-Net* FS (Fine-tune Subset) respectively. For all cases we normalize the images by dividing all pixels by 255. This scales all pixels to lie in the range $[0, 1]$. For the model described in Section 4.2 we set the batch-size to 128 and train the model for a 1000 epochs. Just like the Signal-To-PI model we set the learning rate for the first 300 epochs, next 300 epochs and final 400 epochs to 10^{-3} , 10^{-4} and 10^{-5} respectively. Here too we use Adam optimizer and the Mean-Squared-Error loss function. The training and test loss trends for the different *Image PI-Net* models are shown in Figure 6.

Ground-truth PIs and PIs generated using the above *Image PI-Net* cases for both the *CIFAR10* and *SVHN* are shown in Figures 7 and 8 respectively. For image classification we use *Alexnet* [26] and *Network-in-Network* (*NIN*) [27] as our base models. Topological features like PIs alone are not as powerful as features learnt by most deep learn-

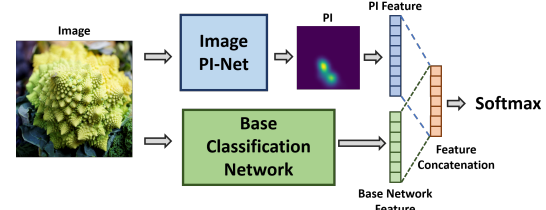


Figure 9. Illustration of the modified base model where we concatenate PI feature with features learnt using the base classification network.

Method	CIFAR10		SVHN	
	Mean±SD	p-Value	Mean±SD	p-Value
Alexnet	80.49±0.30	-	93.08±0.17	-
Alexnet + PI	80.52±0.38	0.8932	93.72±0.10	0.0001
Alexnet + Image PI-Net	81.25±0.49	0.0182	93.83±0.11	<0.0001
Alexnet + Image PI-Net FA	81.23±0.42	0.0125	93.92±0.13	<0.0001
Alexnet + Image PI-Net FS	81.80±0.24	0.0001	93.94±0.13	<0.0001
NIN	84.93±0.13	-	95.83±0.07	-
NIN + PI	85.29±0.30	0.0392	95.75±0.08	0.1309
NIN + Image PI-Net	86.61±0.19	<0.0001	96.04±0.04	0.0004
NIN + Image PI-Net FA	86.62±0.39	<0.0001	95.97±0.05	0.0066
NIN + Image PI-Net FS	86.61±0.40	<0.0001	96.06±0.04	0.0002

Table 3. Image classification results for *CIFAR10* and *SVHN* datasets. Mean±Standard-deviation values are shown over 5 runs. p-values are calculated with respect to the base model.

ing frameworks. This is clearly evident from our earlier experiment in Section 5.1, where a simple 1D CNN applied directly over the time-series data outperforms a MLP that takes in PIs as input. However, from the same section and from past work [40, 12] we know that topological features carry complimentary information that can be exploited to improve the overall classification performance. We too show results using *Alexnet* and *NIN* models in conjunction with PIs that are generated using traditional filtration techniques and using the proposed *Image PI-Net* model. Figure 9 illustrates how we concatenate PIs with the base network feature for image classification.

The network architecture for *Alexnet* and *NIN* models is shown in Table 2. When fusing PIs with the *Alexnet* model, we first pass PIs through two dense layers with ReLU activation and having 1024, 512 units respectively. Each dense layer is followed by a dropout layer with dropout rate 0.2 and batch-normalization. The final PI output is concatenated with the output of the final dropout layer 'drop3' in *Alexnet*. We modify the *NIN* model slightly when fusing PIs. The only change is that we put the global-average-pool layer after 'conv3b', instead of 'conv3c'. We concatenate the PI features with the output of the global-average-pool layer. The classification results are tabulated in Table 3. We see that PIs generated using all variants of the proposed framework help improve the overall classification results for the base models on both datasets. The p-values are calculated for each case with respect to only the base model.

5.3. Robustness to Noise

In this section we create noisy variations of the test set in *CIFAR10* and *SVHN*. In particular we generate noisy images

CIFAR10	Blur					Translation					Gaussian Noise				
	2 × 2	3 × 3	4 × 4	5 × 5	6 × 6	10%	15%	20%	25%	30%	SD 0.02	SD 0.04	SD 0.06	SD 0.08	SD 0.10
Alexnet	71.57±1.80	51.18±2.67	38.14±1.73	31.78±0.95	28.34±0.85	72.83±1.00	68.06±0.94	62.06±1.11	55.48±1.00	49.46±0.77	77.86±0.47	65.10±1.79	48.49±2.75	34.94±2.65	25.98±2.57
Alexnet + PI	68.79±0.90	45.83±1.69	32.50±1.02	26.58±0.93	23.29±0.70	71.30±0.38	66.23±0.38	60.59±0.49	53.97±0.27	48.18±0.64	76.11±0.20	58.52±1.24	39.56±2.32	27.23±2.10	19.59±0.94
Alexnet + Image PI-Net	71.79±0.45	49.65±0.58	35.35±0.67	28.76±0.66	25.64±0.47	73.41±0.28	68.80±0.57	63.05±0.25	56.34±0.39	50.84±0.24	77.46±0.38	60.68±1.94	40.80±3.03	27.04±2.97	19.22±2.38
Alexnet + Image PI-Net FA	71.29±0.60	47.99±1.39	35.24±1.49	29.21±1.27	26.35±0.97	73.24±0.68	68.38±0.47	62.89±0.60	55.95±0.55	50.42±1.05	77.38±0.50	60.92±2.09	40.84±2.65	26.57±2.29	18.54±1.59
Alexnet + Image PI-Net FS	71.38±1.00	47.98±2.63	34.32±1.74	28.07±1.00	25.31±0.46	73.39±0.50	68.52±0.22	62.99±0.35	56.02±0.44	50.28±0.25	77.89±1.12	59.73±3.94	39.10±4.21	25.05±3.05	17.29±1.89
NIN	77.79±0.91	54.98±1.45	38.39±0.84	30.21±0.55	26.23±0.62	80.28±0.20	77.93±0.44	74.64±0.38	70.85±0.38	65.98±0.46	81.21±0.55	66.65±2.15	48.37±3.35	33.64±3.49	24.03±2.85
NIN + PI	76.93±0.73	49.24±1.95	32.19±1.57	25.17±1.69	21.69±1.66	80.35±0.24	77.57±0.34	74.41±0.27	70.51±0.31	65.31±0.22	81.08±0.70	64.09±2.32	44.08±3.90	28.81±3.55	19.48±2.46
NIN + Image PI-Net	77.70±0.78	49.75±1.38	33.37±1.15	26.12±0.43	23.29±0.65	81.40±0.38	78.83±0.38	75.92±0.43	72.05±0.40	66.90±0.51	82.69±0.37	65.91±2.27	45.19±3.87	29.43±3.53	19.95±2.48
NIN + Image PI-Net FA	77.43±0.98	50.52±1.61	34.29±1.98	26.86±1.93	23.90±1.87	81.19±0.28	78.61±0.35	75.60±0.44	71.66±0.42	66.60±0.19	82.68±0.27	66.14±1.38	46.80±2.35	31.92±2.92	22.86±2.68
NIN + Image PI-Net FS	78.50±1.05	51.39±2.06	34.58±1.75	26.84±1.22	23.11±1.33	81.76±0.44	79.24±0.48	76.40±0.36	72.53±0.58	67.49±0.40	82.48±0.25	65.74±1.17	44.67±1.26	28.25±1.19	19.42±0.92
SVHN	Blur					Translation					Gaussian Noise				
	2 × 2	3 × 3	4 × 4	5 × 5	6 × 6	10%	15%	20%	25%	30%	SD 0.02	SD 0.04	SD 0.06	SD 0.08	SD 0.10
Alexnet	92.83±0.14	92.70±0.16	91.42±0.14	89.63±0.17	85.73±0.25	88.42±0.23	80.98±0.43	68.39±0.55	55.49±0.70	45.14±0.49	91.14±0.49	78.33±2.23	59.26±3.02	44.89±2.77	35.74±2.33
Alexnet + PI	93.61±0.13	93.36±0.14	92.19±0.08	90.21±0.08	86.08±0.21	90.05±0.06	83.54±0.21	72.16±0.46	59.52±0.24	48.46±0.45	92.33±0.19	85.07±1.26	72.41±2.18	60.38±2.67	49.29±2.84
Alexnet + Image PI-Net	93.64±0.13	93.41±0.15	92.32±0.16	90.44±0.10	86.53±0.10	90.10±0.33	83.74±0.52	72.07±0.65	59.60±0.68	48.52±0.48	92.80±0.23	87.26±0.98	75.28±1.89	61.13±2.29	48.33±2.45
Alexnet + Image PI-Net FA	93.74±0.14	93.52±0.10	92.27±0.07	90.52±0.08	86.55±0.14	90.29±0.12	83.99±0.19	72.60±0.39	59.82±0.36	48.71±0.23	93.01±0.15	88.09±0.33	78.28±1.57	66.75±2.96	55.74±3.87
Alexnet + Image PI-Net FS	93.68±0.15	93.53±0.15	92.41±0.10	90.53±0.14	86.59±0.28	90.35±0.09	83.96±0.19	72.44±0.36	59.74±0.31	48.74±0.36	92.89±0.18	86.98±0.89	74.96±2.46	61.35±3.36	49.25±3.42
NIN	95.68±0.06	95.40±0.05	94.47±0.08	92.75±0.10	89.39±0.21	94.52±0.13	92.25±0.11	87.25±0.21	79.40±0.37	69.50±0.45	95.39±0.09	92.81±0.16	86.99±0.44	79.34±0.68	70.81±0.75
NIN + PI	95.65±0.04	95.27±0.09	94.30±0.12	92.36±0.12	88.61±0.20	94.46±0.09	92.10±0.10	86.87±0.20	78.56±0.22	68.24±0.22	95.08±0.09	91.97±0.29	85.48±0.57	76.95±0.90	68.14±0.63
NIN + Image PI-Net	95.88±0.04	95.62±0.06	94.67±0.11	92.87±0.09	89.41±0.19	94.79±0.07	92.35±0.04	87.41±0.15	79.58±0.19	69.77±0.35	95.52±0.08	92.88±0.25	86.98±0.52	78.93±0.69	70.16±1.07
NIN + Image PI-Net FA	95.83±0.05	95.54±0.08	94.63±0.11	92.79±0.19	89.23±0.21	94.77±0.11	92.43±0.15	87.54±0.26	79.89±0.36	70.02±0.53	95.43±0.09	92.40±0.49	85.85±0.69	77.63±0.97	68.21±1.34
NIN + Image PI-Net FS	95.92±0.05	95.62±0.09	94.69±0.06	92.94±0.08	89.44±0.17	94.81±0.11	92.40±0.16	87.48±0.16	79.64±0.30	69.75±0.11	95.53±0.11	92.53±0.16	86.13±0.34	77.83±0.52	68.24±0.38

Table 4. Image classification results for CIFAR10 (top) and SVHN (bottom) datasets when subjected to different levels of blur, affine translation and Gaussian noise. When fusing with the base model, PIs generated using the Image PI-Net model are most useful on the SVHN dataset for all noise variations. They are particularly useful for affine translation noise on the CIFAR10 dataset.

Method	Mean±SD (10 ⁻³ seconds)	
	CIFAR10 (50,000 images)	SVHN (73,257 images)
Conventional TDA - CPU	146.50±3.83	105.03±3.57
Image PI-Net - GPU	2.52±0.02	2.19±0.02

Table 5. Comparison of the average time taken to compute PIs for one image using conventional TDA tools and the proposed Image PI-Net model. The time reported is averaged over all images present in the training set of each dataset.

with different levels of blur, affine translation and Gaussian noise. We evaluate the performance of the base models described in Section 5.2 on these noisy image variants. Both *Alexnet* and *NIN* are evaluated alone and after fusion with PIs. The PIs are generated again for the noisy images using conventional TDA tools and the proposed Image PI-net framework. Note that these models were trained using just clean images from the dataset and are not retrained on noisy images. For blur we use an averaging filter and consider the following 5 kernel sizes - (2 × 2), (3 × 3), (4 × 4), (5 × 5), (6 × 6). For affine transformation, we translate the image within 10%, 15%, 20%, 25%, 30% percentage ranges. In the case of Gaussian noise, we add Gaussian noise to the original image with different levels of standard-deviation - 0.02, 0.04, 0.06, 0.08 and 0.10. The results are tabulated in Table 4. We observe that fusing PIs generated using the Image PI-net model is beneficial on all cases for *Alexnet* and *NIN* on the *SVHN* dataset, and for affine translation noise case on the *CIFAR10* dataset.

5.4. Computation Time to Generate PIs

We used 4 NVIDIA GeForce GTX Titan Xp graphic cards, each with 12GB memory to train and evaluate all deep learning models. All other tasks were carried out on a

standard Intel i7 CPU using Python with a working memory of 32GB. We use the Scikit-TDA software to compute PDs and PIs [36]. Table 5 shows the average time taken by conventional TDA methods using one CPU and the proposed *Image PI-Net* framework on just one GPU, to extract PI for one image. The average is computed over all images present in the training set of the dataset. Using the Image PI-Net model, we see an effective speed up of two orders of magnitude in the computation time. We also check the time taken to compute PIs when the entire training set is passed into the Image PI-Net model as a single batch. For the entire training set it takes about 9.77±0.08 seconds for *CIFAR10* and 12.93±0.05 seconds for *SVHN*. This is a fraction of the time compared to the time it takes using conventional TDA tools. So far it had been impossible to compute PIs at real-time using conventional TDA approaches. However, the proposed framework allows us to easily compute PIs in real-time thereby opening doors to new real-time applications for TDA.

6. Conclusion and Future Work

In this paper we took the first step in using deep learning to extract topological feature representations. We developed a differentiable and effective architecture called PI-Net to extract PIs directly from data. PI-Net has a significantly lower computational complexity compared to using conventional topological tools. We show good results on different time-series and image datasets, and also test the robustness of different base classification networks together with PIs generated using PI-Net for different kinds of noise added to the data.

For future work we would like to explore more sophisti-

cated deep learning architectures that can allow us to learn mappings between higher dimensional data and their corresponding topological feature representations. We would also like to see how deep learning can be further used to generate other kinds of topological representations. Also, conventional TDA tools are invariant to small perturbations on the input data space. Now that we are able to generate approximations of topological representations, it would be interesting to use the proposed framework in a setting that is resistant to adversarial attacks which is major issue faced by current deep neural networks.

7. Acknowledgements

This work was supported in part by NSF CAREER grant 1452163 and ARO grant number W911NF-17-1-0293.

References

- [1] H. Adams, T. Emerson, M. Kirby, R. Neville, C. Peterson, P. Shipman, S. Chepushtanova, E. Hanson, F. Motta, and L. Ziegelmeier. Persistence images: A stable vector representation of persistent homology. *Journal of Machine Learning Research*, 18(8):1–35, 2017. [2](#), [3](#)
- [2] H. Adams, A. Tausz, and M. Vejdemo-Johansson. Javaplex: A research software package for persistent (co) homology. In *International Congress on Mathematical Software*, pages 129–136. Springer, 2014. [2](#)
- [3] R. Anirudh, V. Venkataraman, K. Natesan Ramamurthy, and P. Turaga. A riemannian framework for statistical analysis of topological persistence diagrams. In *The IEEE Conference on Computer Vision and Pattern Recognition Workshops*, pages 68–76, 2016. [2](#)
- [4] U. Bauer, M. Kerber, and J. Reininghaus. Distributed computation of persistent homology. In *Proceedings of the Workshop on Algorithm, Engineering and experiments*, pages 31–38. SIAM, 2014. [2](#)
- [5] P. Bubenik. Statistical topological data analysis using persistence landscapes. *The Journal of Machine Learning Research*, 16(1):77–102, 2015. [2](#)
- [6] P. Bubenik and J. Holcomb. Statistical inferences from the topology of complex networks. Technical report, Cleveland State University, Cleveland, United States, 2016. [1](#), [2](#)
- [7] Z. Cang and G.-W. Wei. Topologynet: Topology based deep convolutional and multi-task neural networks for biomolecular property predictions. *PLoS Computational Biology*, 13(7), 2017. [2](#)
- [8] H. Chintakunta, T. Gentimis, R. Gonzalez-Diaz, M.-J. Jimenez, and H. Krim. An entropy-based persistence barcode. *Pattern Recognition*, 48(2):391–401, 2015. [2](#)
- [9] F. Chollet et al. Keras. <https://keras.io>, 2015. [4](#)
- [10] M. K. Chung, P. Bubenik, and P. T. Kim. Persistence diagrams of cortical surface data. In *International Conference on Information Processing in Medical Imaging*, pages 386–397. Springer, 2009. [2](#)
- [11] Y. Dabaghian, F. Mémoli, L. Frank, and G. Carlsson. A topological paradigm for hippocampal spatial map formation using persistent homology. *PLoS Computational Biology*, 8(8):1–14, 2012. [2](#)
- [12] T. K. Dey, S. Mandal, and W. Varcho. Improved Image Classification using Topological Persistence. In *Vision, Modeling & Visualization*. The Eurographics Association, 2017. [2](#), [7](#)
- [13] C. Dong, C. C. Loy, K. He, and X. Tang. Learning a deep convolutional network for image super-resolution. In *European Conference on Computer Vision*, pages 184–199. Springer, 2014. [1](#), [2](#), [3](#)
- [14] H. Edelsbrunner and J. Harer. *Computational topology: an introduction*. American Mathematical Society, 2010. [1](#), [2](#)
- [15] H. Edelsbrunner, D. Letscher, and A. Zomorodian. Topological persistence and simplification. *Discrete & Computational Geometry*, 28(4):511–533, 2002. [2](#)
- [16] D. Eigen, C. Puhrsch, and R. Fergus. Depth map prediction from a single image using a multi-scale deep network. In *Advances in Neural Information Processing Systems*, pages 2366–2374, 2014. [1](#), [2](#), [3](#)
- [17] M. Ferri. Why topology for machine learning and knowledge extraction? *Machine Learning and Knowledge Extraction*, 1(1):115–120, 2018. [1](#)
- [18] M. Gabella, N. Afambo, S. Ebli, and G. Spreemann. Topology of learning in artificial neural networks. *arXiv preprint arXiv:1902.08160*, 2019. [1](#), [2](#)
- [19] R. B. Gabriellsson and G. Carlsson. Exposition and interpretation of the topology of neural networks. *arXiv preprint arXiv:1810.03234*, 2018. [1](#), [2](#)
- [20] R. Girshick, J. Donahue, T. Darrell, and J. Malik. Rich feature hierarchies for accurate object detection and semantic segmentation. In *Proceedings of the IEEE Conference on Computer Vision and Pattern Recognition*, pages 580–587, 2014. [1](#)
- [21] K. Grill-Spector and R. Malach. The human visual cortex. *Annu. Rev. Neurosci.*, 27:649–677, 2004. [3](#)
- [22] K. He, X. Zhang, S. Ren, and J. Sun. Deep residual learning for image recognition. In *Proceedings of the IEEE Conference on Computer Vision and Pattern Recognition*, pages 770–778, 2016. [3](#)
- [23] K. Heath, N. Gelfand, M. Ovsjanikov, M. Aanjaneya, and L. J. Guibas. Image webs: Computing and exploiting connectivity in image collections. In *IEEE Conference on Computer Vision and Pattern Recognition*, 2010. [2](#)
- [24] C. Hofer, R. Kwitt, M. Niethammer, and A. Uhl. Deep learning with topological signatures. In *Advances in Neural Information Processing Systems*, pages 1634–1644. 2017. [2](#)
- [25] A. Krizhevsky and G. Hinton. Learning multiple layers of features from tiny images. Technical report, Citeseer, 2009. [5](#), [6](#)
- [26] A. Krizhevsky, I. Sutskever, and G. E. Hinton. Imagenet classification with deep convolutional neural networks. In *Advances in Neural Information Processing Systems*, pages 1097–1105, 2012. [1](#), [2](#), [3](#), [5](#), [7](#)
- [27] M. Lin, Q. Chen, and S. Yan. Network in network. *arXiv preprint arXiv:1312.4400*, 2013. [2](#), [3](#), [5](#), [7](#)
- [28] J. Long, E. Shelhamer, and T. Darrell. Fully convolutional networks for semantic segmentation. In *Proceedings of the IEEE Conference on Computer Vision and Pattern Recognition*, pages 3431–3440, 2015. [1](#), [2](#), [3](#)

- [29] Y. Netzer, T. Wang, A. Coates, A. Bissacco, B. Wu, and A. Y. Ng. Reading digits in natural images with unsupervised feature learning. 2011. 5, 6
- [30] D. Pachauri, C. Hinrichs, M. K. Chung, S. C. Johnson, and V. Singh. Topology-based kernels with application to inference problems in alzheimer’s disease. *IEEE transactions on Medical Imaging*, 30(10):1760–1770, 2011. 2
- [31] J. A. Perea and J. Harer. Sliding windows and persistence: An application of topological methods to signal analysis. *Foundations of Computational Mathematics*, 15(3):799–838, 2015. 2
- [32] K. N. Ramamurthy, K. Varshney, and K. Mody. Topological data analysis of decision boundaries with application to model selection. In *Proceedings of the International Conference on Machine Learning*, pages 5351–5360, 2019. 1, 2
- [33] J. Reininghaus, S. Huber, U. Bauer, and R. Kwitt. A stable multi-scale kernel for topological machine learning. In *IEEE Conference on Computer Vision and Pattern Recognition*, 2015. 2
- [34] B. Rieck, M. Togninalli, C. Bock, M. Moor, M. Horn, T. Gumbsch, and K. Borgwardt. Neural persistence: A complexity measure for deep neural networks using algebraic topology. In *International Conference on Learning Representations*, 2019. 1, 2
- [35] D. Rouse, A. Watkins, D. Porter, J. Harer, P. Bendich, N. Strawn, E. Munch, J. DeSena, J. Clarke, J. Gilbert, et al. Feature-aided multiple hypothesis tracking using topological and statistical behavior classifiers. In *SPIE Defense+Security*, 2015. 2
- [36] N. Saul and C. Tralie. Scikit-TDA: Topological data analysis for python. <https://doi.org/10.5281/zenodo.2533369>, 2019. 2, 3, 8
- [37] D. Silver, A. Huang, C. J. Maddison, A. Guez, L. Sifre, G. Van Den Driessche, J. Schrittwieser, I. Antonoglou, V. Panneershelvam, M. Lanctot, et al. Mastering the game of go with deep neural networks and tree search. *nature*, 529(7587):484, 2016. 3
- [38] K. Simonyan and A. Zisserman. Very deep convolutional networks for large-scale image recognition. *arXiv preprint arXiv:1409.1556*, 2014. 3
- [39] G. Singh, F. Memoli, T. Ishkhanov, G. Sapiro, G. Carlsson, and D. L. Ringach. Topological analysis of population activity in visual cortex. *Journal of Vision*, 2008. 2
- [40] A. Som, K. Thopalli, K. Natesan Ramamurthy, V. Venkataraman, A. Shukla, and P. Turaga. Perturbation robust representations of topological persistence diagrams. In *Proceedings of the European Conference on Computer Vision*, pages 617–635, 2018. 2, 7
- [41] S. Srinivas, R. K. Sarvadevabhatla, K. R. Mopuri, N. Prabhu, S. S. Kruthiventi, and R. V. Babu. A taxonomy of deep convolutional neural nets for computer vision. *Frontiers in Robotics and AI*, 2:36, 2016. 3
- [42] C. Szegedy, W. Liu, Y. Jia, P. Sermanet, S. Reed, D. Anguelov, D. Erhan, V. Vanhoucke, and A. Rabinovich. Going deeper with convolutions. In *Proceedings of the IEEE Conference on Computer Vision and Pattern Recognition*, pages 1–9, 2015. 3
- [43] C. J. Tralie and J. A. Perea. (quasi) periodicity quantification in video data, using topology. *SIAM Journal on Imaging Sciences*, 11(2):1049–1077, 2018. 2
- [44] V. Venkataraman, K. N. Ramamurthy, and P. Turaga. Persistent homology of attractors for action recognition. In *IEEE International Conference on Image Processing*, pages 4150–4154. IEEE, 2016. 2
- [45] J. Walker, A. Gupta, and M. Hebert. Dense optical flow prediction from a static image. In *Proceedings of the IEEE International Conference on Computer Vision*, pages 2443–2451, 2015. 1, 2, 3
- [46] Q. Wang, S. Lohit, M. J. Toledo, M. P. Buman, and P. Turaga. A statistical estimation framework for energy expenditure of physical activities from a wrist-worn accelerometer. In *Annual International Conference of the IEEE Engineering in Medicine and Biology Society*, pages 2631–2635. IEEE, 2016. 5, 11, 12
- [47] X. Wang, D. Fouhey, and A. Gupta. Designing deep networks for surface normal estimation. In *Proceedings of the IEEE Conference on Computer Vision and Pattern Recognition*, pages 539–547, 2015. 1, 2, 3
- [48] J. Yosinski, J. Clune, Y. Bengio, and H. Lipson. How transferable are features in deep neural networks? In *Advances in Neural Information Processing Systems*, pages 3320–3328, 2014. 3
- [49] M. Zhang and A. A. Sawchuk. USC-HAD: a daily activity dataset for ubiquitous activity recognition using wearable sensors. In *Proceedings of the ACM Conference on Ubiquitous Computing*, pages 1036–1043. ACM, 2012. 5, 11, 12, 13
- [50] N. Zhang, J. Donahue, R. Girshick, and T. Darrell. Part-based R-CNNs for fine-grained category detection. In *European Conference on Computer Vision*, pages 834–849. Springer, 2014. 1
- [51] N. Zhang, M. Paluri, M. Ranzato, T. Darrell, and L. Bourdev. Panda: Pose aligned networks for deep attribute modeling. In *Proceedings of the IEEE Conference on Computer Vision and Pattern Recognition*, pages 1637–1644, 2014. 1
- [52] B. Zhou, A. Lapedriza, J. Xiao, A. Torralba, and A. Oliva. Learning deep features for scene recognition using places database. In *Advances in Neural Information Processing Systems*, pages 487–495, 2014. 1

Appendix

Confusion Matrix for Time-series Human Activity Recognition

Here we show the confusion matrices for a few of the methods listed in Table 1. Specifically we show the confusion matrix for the Multi Layer Perceptron (MLP) method on the 19-dimensional statistical feature (SF), persistence image (PI) obtained using conventional topological data analysis (TDA) tools and PI computed using the proposed PI-Net model. We show these for both the GeneActiv [46] and USC-HAD [49] datasets in Figures 10 and 12 respectively. We also show the confusion matrices for the 1-dimensional convolutional neural network (1D CNN) both alone and in fusion with the two PI variants in Figures 11 and 13 respectively. For the MLP classifier we observe PI features being more informative than the SF method. We also observe that fusing PIs with more powerful classifiers like 1D CNNs helps improve the overall classification performance. We used the same Signal PI-Net model trained on the GeneActiv dataset to extract PIs for the USC-HAD dataset, *i.e.* we do not fine-tune the model again using the USC-HAD dataset.

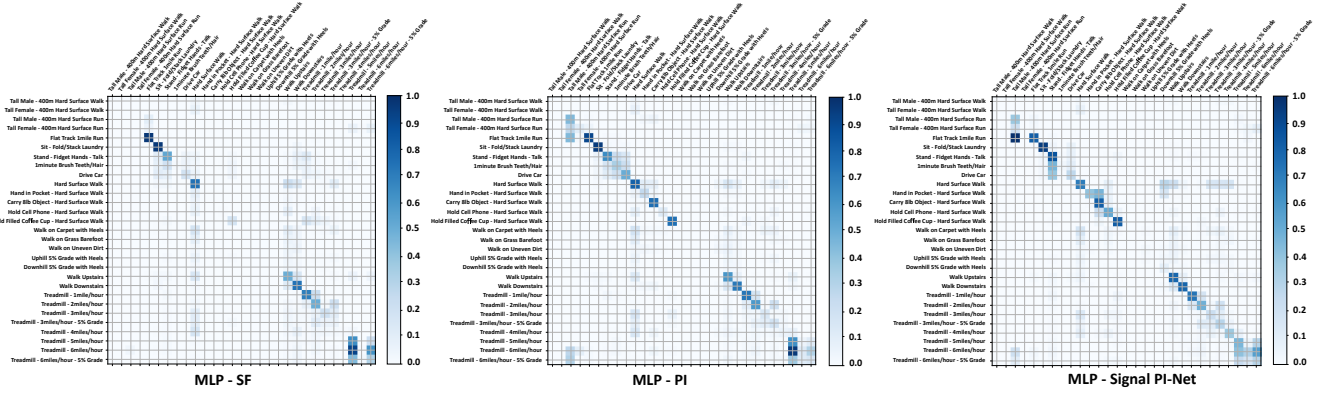


Figure 10. Confusion matrices for **MLP - SF** [46] (left), **MLP - PI** (middle) and **MLP - Signal PI-Net** (right) methods on the GeneActiv dataset [46] listed in Table 1.

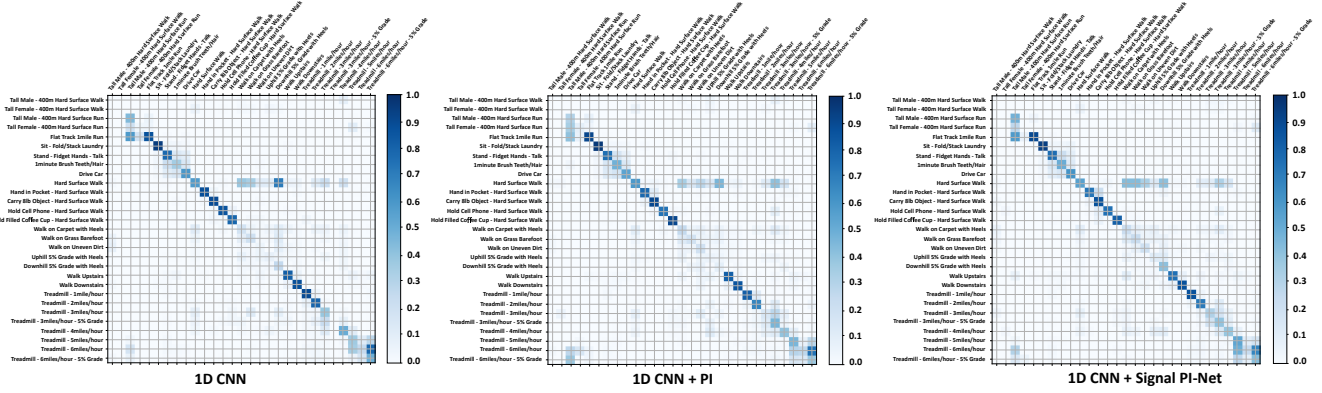


Figure 11. Confusion matrices for **1D CNN** (left), **1D CNN + PI** (middle) and **1D CNN + Signal PI-Net** (right) methods on the GeneActiv dataset [46] listed in Table 1.

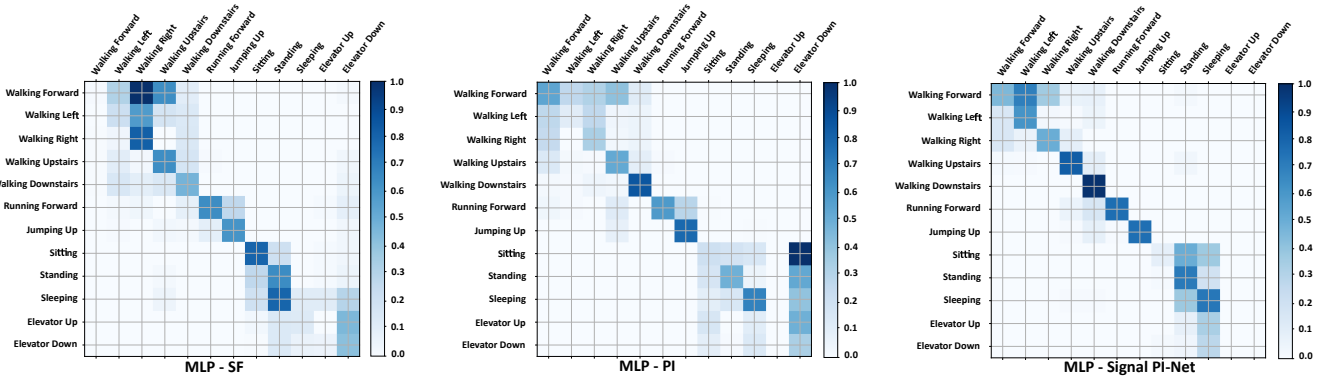


Figure 12. Confusion matrices for **MLP - SF** (left), **MLP - PI** (middle) and **MLP - Signal PI-Net** (right) methods on the USC-HAD dataset [49] listed in Table 1.

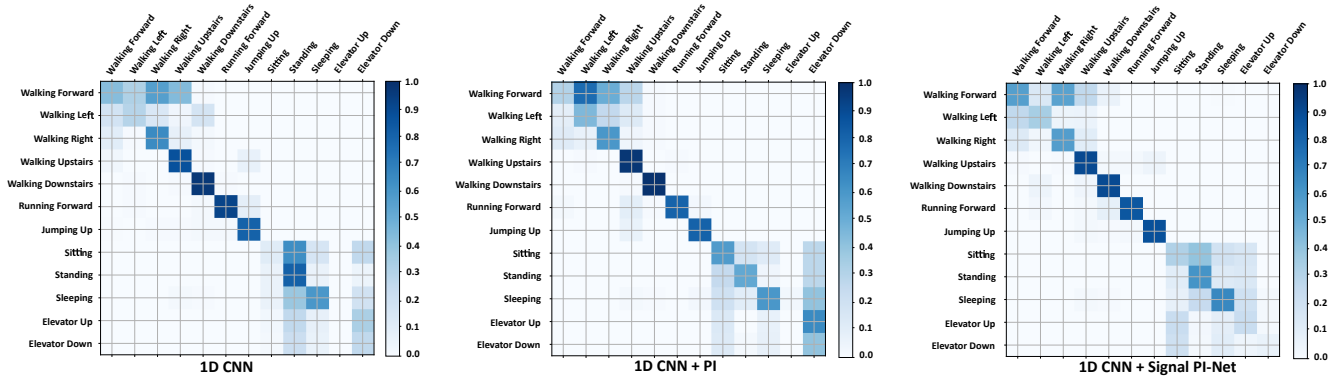


Figure 13. Confusion matrices for **1D CNN** (left), **1D CNN + PI** (middle) and **1D CNN + Signal PI-Net** (right) methods for on USC-HAD dataset [49] listed in Table 1.